CFA/VISHNO 2016

Contrôle des vibrations par surfaces résonantes : Un parallèle entre l'acoustique et l'élastodynamique

L. Schwan[a], O. Umnova[a], C. Boutin[b] et M. Dietz[c]
[a]University of Salford, Acoustics Research Centre, Newton Building, M5 4WT Salford, UK
[b]LGCB - UMR CNRS 5513 - CeLyA, Ecole Nationale des Travaux Publics de l'Etat, Rue Maurice Audin, 69518 Vaulx-En-Velin Cedex, France, Metropolitan
[c]Univ. of Bristol, Department of Civil Engineering, University Walk, BS8 1TR Bristol, UK
logan.schwan@gmail.com

Effects from micro-structured surfaces with inner resonance, that is resonant surfaces, are investigated in both acoustics and elastodynamics. Their behaviour is described in terms of effective boundary conditions derived by means of two-scale asymptotic homogenization. The model is validated by comparing its results with shaking table measurements in elastodynamics and impedance tube and anechoic chamber measurements in acoustics. The model is also validated numerically against Multiple Scattering Theory in acoustics. It is shown that elastodynamic resonant surfaces can depolarize mechanical waves in homogeneous media, and that acoustics resonant surfaces are efficient for total sound absorption in the deep sub-wavelength regime (lattice size smaller than wavelength/27).

1 Introduction

An economic way to control vibrations in homogeneous media is to control boundary conditions : the internal structure thus remains unperturbed and the surface treatment requires less materials than that of the entire volume.

The present study focuses on vibration control through micro-structured resonant surfaces in acoustics and elastodynamics. In particular, it aims at investigating the similarities and differences of resonant surfaces in these domains. Although both acoustics and elastodynamics are parts of continuum dynamics, acoustics deals mostly with wave propagation in fluids, while elastodynamics considers propagation in solids. In acoustics the main descriptor is pressure, which is a scalar quantity. In elastodynamics a vector particle displacement is used to describe the wave phenomena.

Nevertheless, whether in acoustics or in elastodynamics, the concept of resonant surface remains the same : it is made up of the two-dimensional Σ-periodic arrangement of linear resonators at the plane boundary Γ (outward normal $\mathbf{n}$) of the medium. The propagation of small perturbations is studied in the linear harmonic regime at frequencies $\omega/(2\pi)$ (time factor $e^{-\mathrm{i}\omega t}$) close to the eigenfrequency $\omega_o/(2\pi)$ of the resonators. In that frequency range, a scale separation is assumed, whereby the wavelength $\lambda = 2\pi/k$ is much larger than the characteristic size ℓ of the representative element of the array. This scale separation is quantified by the small scale parameter $\epsilon = 2\pi\ell/\lambda \ll 1$. The physics of such micro-structured surfaces is distinct from that of corrugated surfaces, that display no resonance in the low frequency range, and that of phononic crystal surfaces for which the wavelength is of the order of the lattice size.

Due to the deep sub-wavelength regime, small-scale perturbations introduced in the fields by the micro-structures remain localized nearby the resonant surface, and form a locally-periodic boundary layer. Taking advantage of the 2-D periodicity and of the scale separation, the method of two-scale asymptotic homogenization [1, 2] is applied to analyse that boundary layer. This method (ordinary used to derive the equivalent behaviour of heterogeneous bulk media) enables to describe the resonant surface effect by an effective boundary condition with unconventional frequency-dependent properties [3]. Analytical predictions are straightforward and make the design of resonant surfaces easily adjustable. Experimental prototypes are designed, which confirm, both in acoustics and elastodynamics, the efficiency and robustness of this principle to control waves in the medium.

2 Homogenization of resonant surface

The derivation of the effective boundary conditions for the resonant surface are presented in this section. The elastodynamic model of Boutin & Roussillon [3] is briefly recalled and extended to acoustic resonant surfaces. That allows us to underline the differences between elastodynamics and acoustics, despite their common roots in continuum dynamics.

2.1 Analogy and duality between acoustics and elastodynamics

The homogenization of resonant surfaces in acoustics and elastodynamics can be achieved in a similar way, exploiting the following analogy between them. The field of interest is the pressure field p in acoustics, and the displacement field $\mathbf{u}$ in elastodynamics. Their first spatial derivatives are related to a flux : in acoustics, the gradient $\mathbf{grad}\, p$ is related to the particle velocity $\mathbf{v}$ through the momentum conservation ; while the deformation tensor $\mathbf{e}(\mathbf{u}) = (\mathbf{grad}\,\mathbf{u} + {}^t\mathbf{grad}\,\mathbf{u})/2$ is related to the stress tensor $\boldsymbol{\sigma}$ through the elasticity relation in elastodynamics :

$$\mathrm{i}\omega\mathbf{v} = \rho_e^{-1}\mathbf{grad}\, p \quad ; \qquad \boldsymbol{\sigma} = C : \mathbf{e}(\mathbf{u}) \; ; \tag{1}$$

where $\rho_e = 1.213$ kg/m^3 is the air density and C is the elasticity tensor (order 4). The balance of flux in the medium is then stated by the mass conservation in acoustics, and by the dynamic equilibrium in elastodynamics :

$$\mathrm{div}(\mathrm{i}\omega\mathbf{v}) = -B^{-1}\omega^2 p \quad ; \qquad \mathrm{div}(\boldsymbol{\sigma}) = -\rho\omega^2\mathbf{u} \; ; \tag{2}$$

where B is air bulk modulus and ρ is the density of the elastic medium. Equations (1) and (2) bears testament to a strong analogy between acoustics and elastodynamics, but also underlies the stress/displacement duality between them.

2.2 Two-scale phenomena

The scale separation $\epsilon = 2\pi\ell/\lambda \ll 1$ introduces two characteristic lengths in the system : the macroscopic size $L = \lambda/(2\pi)$ of the long-wavelength field and the lattice size $\ell = O(\epsilon L)$ of the micro-structures arrangement. Excited by the wavefield (acoustic pressure or elastic displacement) that prevails in the homogeneous medium $\mathcal{M}$, the micro-structures of the resonant surface act as mutually-interacting secondary sources and produce an heterogeneous distribution of flux at the boundary of the medium (normal particle velocity v_r in acoustics or surface stress $\mathbf{t}$ in elastodynamics). That flux distribution is locally Σ-periodic while being modulated at the long-wavelength scale (forced by the long-wavelength field). The long-wavelength field, which displays significant variations upon distances $O(L)$, cannot balance the two-scale flux distribution on its own,

because of a scale-mismatch with the local periodicity. To fulfil the scale-transition between the long-wavelength field and the sub-wavelength resonator arrangement, a boundary layer is formed in the vicinity of the surface (pressure $p^\star$ and particle velocity $\mathbf{v}^\star$ in acoustics ; displacement $\mathbf{u}^\star$ and stress $\boldsymbol{\sigma}^\star$ in elastodynamics). Superimposed upon the long-wavelength field to satisfy the locally-periodic boundary conditions, and localized near the resonant surface, the Boundary Layer (BL) is made of evanescent waves which fade away at some distance from the surface.

2.3 Homogenization method

The description of the resonant surface by an effective boundary condition relies on the analysis of the boundary layer. Following the method described by Sánchez-Palencia [1] and adapted to resonant surfaces in [3], the homogenization procedure is based on two main steps : the two-scale description of space and the asymptotic expansion of the fields.

To describe field variations at both long-wavelength and deep sub-wavelength scales, two space-variables are used, linked by the scale ratio ϵ : the macro-variable $\mathbf{x}$ and the micro-variable $\mathbf{y} = \epsilon^{-1}\mathbf{x}$. The long-wavelength fields depend only on $\mathbf{x}$ while the boundary layer fields and the flux produced by the resonators at the boundary depend on both variables $\mathbf{x}$ and $\mathbf{y}$. The differentiation of the fields is modified accordingly using both space variables $\mathbf{x}$ and $\mathbf{y}$; for instance $\mathbf{grad} = \mathbf{grad}_\mathbf{x} + \epsilon^{-1}\mathbf{grad}_\mathbf{y}$ where $\mathbf{grad}_\mathbf{x}$ and $\mathbf{grad}_\mathbf{y}$ denote the gradients with respect to $\mathbf{x}$ and $\mathbf{y}$. The space-variables are defined in the Cartesian coordinate system $(\mathbf{e}_1, \mathbf{e}_2, \mathbf{e}_3)$, with $\mathbf{e}_3 = -\mathbf{n}$ being the inward normal. In the local description, that is with the micro-variable $\mathbf{y}$, the origin O of the local frame is chosen at the centre of the period Σ.

The physical fields are expanded asymptotically in powers of ϵ, that is, for instance, $p = p^{(0)} + \epsilon p^{(1)} + \epsilon^2 \dots$ for the pressure field p, where orders are indicated in superscripts between brackets. The expansions are substituted in the governing equations (mass and momentum conservation and rheological relations) and boundary conditions. Terms of equal powers are collected, providing problems that are solved in increasing order of ϵ-powers.

2.4 Physics at leading order

Without providing the full derivation (see [3, 4] for that purpose), this paragraph aims at giving the most significant results found at the leading order (power ϵ^0) and which will be used in the sequel.

First of all, it is shown that the BL fields are one order smaller in amplitude than the long-wavelength field (that is, $p^{\star(0)} = 0$ in acoustics, $\mathbf{u}^{\star(0)} = \mathbf{0}$ in elastodynamics) and thus can be neglected in the leading order description. In other words, the long-wavelength field prevails at the leading order.

Secondly, the balance of flux in the boundary layer is shown to be given by a locally incompressible flow in acoustics, and a locally quasi-static state in elastodynamics :

$$\mathrm{div}_\mathbf{y}(\mathbf{v}^{\star(0)}) = 0 \quad ; \qquad \mathrm{div}_\mathbf{y}(\boldsymbol{\sigma}^{\star(0)}) = 0\,. \tag{3}$$

Associated with the conditions of local periodicity and evanescence of the BL fields $\mathbf{v}^{\star(0)}$ and $\boldsymbol{\sigma}^{\star(0)}$, the following boundary conditions are found for the long-wavelength fields at each period Σ :

$$\mathbf{v}^{(0)} \cdot \mathbf{n} = -\frac{Q^{(0)}}{|\Sigma|} \quad ; \qquad \boldsymbol{\sigma}^{(0)}.\mathbf{n} = \frac{\mathbf{F}^{(0)}}{|\Sigma|}\,; \tag{4}$$

where $Q^{(0)} = \int v_r^{(0)}\, dS$ is the acoustic flux pulsed out by the resonators at Σ, and $\mathbf{F}^{(0)} = \int \mathbf{t}^{(0)}\, dS$ is the force exerted by the resonators on the elastic medium at Σ. Note that, due to the stress/displacement duality noted previously, acoustic resonators affect the mass conservation, while mechanical resonators affect the balance of stress.

Finally, due to the linearity of the resonators, they respond to the prevailing long-wavelength field ($p^{(0)}$ in acoustics, $\mathbf{u}^{(0)}$ in elastodynamics) through a frequency-dependent acoustic admittance Y or mechanical impedance matrix $\mathbb{Z}$, that is $Q^{(0)} = Yp^{(0)}$ and $\mathbf{F}^{(0)} = \mathbb{Z}\mathbf{u}^{(0)}$. As a result, the long-wavelength fields are governed by the following equations in the medium $\mathcal{M}$ and at its boundary Γ (the superscrips (0) are omitted here and in the sequel) :

$$\begin{cases} \mathrm{div}\left[\rho_e^{-1}\mathbf{grad}\, p\right] = -B^{-1}\omega^2 p & \text{in } \mathcal{M} \\ \left[\rho_e^{-1}\mathbf{grad}\, p\right]\cdot\mathbf{n} = \mathrm{i}\omega\Upsilon p & \text{at } \Gamma \end{cases} \tag{5}$$

in acoustics, and

$$\begin{cases} \mathrm{div}\,[C : \mathbf{e}(\mathbf{u})] = -\rho\omega^2\mathbf{u} & \text{in } \mathcal{M} \\ [C : \mathbf{e}(\mathbf{u})]\,.\mathbf{n} = \mathbb{Z}_\Gamma\mathbf{u} & \text{at } \Gamma \end{cases} \tag{6}$$

in elastodynamics, where $\Upsilon = -Y/|\Sigma|$ and $\mathbb{Z}_\Gamma = \mathbb{Z}/|\Sigma|$ are the effective acoustic admittance and elastodynamic surface impedance matrix of the resonant surfaces. Consequently, frequency-dependent effects can arise from the resonant admittance Υ or surface impedance $\mathbb{Z}_\Gamma$ (despite the elasticity of the media). Moreover, in elastodynamics, the matrix $\mathbb{Z}_\Gamma$ can be anisotropic (depending on the properties of the mechanical resonators) thus producing anisotropic phenomena in an otherwise isotropic medium.

3 Elastodynamic resonant surface

To observe depolarization of waves by the resonant surface [3, 5, 6], an experimental prototype is designed using the homogenization model, and experimental results are compared to the theoretical ones.

3.1 Experimental prototype

The anisotropic resonant surface consists of 37 resonators arranged periodically with the spacing $\ell = 5$ cm see Fig.1(a). Each resonator (mass $m_t = 0.849$ kg) consists of a rectangular aluminium sheet clamped at its long edge between two angle bars adhered to the elastic substrate. The resonators respond to any horizontal motion by resonating in bending with out-of-plane excitation (direction $\mathbf{e}_1$), but remains inert with in-plane excitation ($\mathbf{e}_2$ orthogonal to $\mathbf{e}_1$). In the bending direction $\mathbf{e}_1$ and around its first mode, the resonant sheet (18.3 cm-high outside the angle-bars, 0.5 mm-thick) is characterized by the sheet's fundamental frequency $\omega_o^{[1]}/(2\pi) = 8.45$ Hz, modal mass at the first mode $m_o^{[1]} = 0.266$ kg (61.3% of the bending mass), and weak damping $\xi_o \sim 3.8\%$. The complementary mass $m_i^{[1]} = m_t - m_o^{[1]}$ accounts for the inert mass associated with inactivated modes. In the orthogonal direction $\mathbf{e}_2$, the

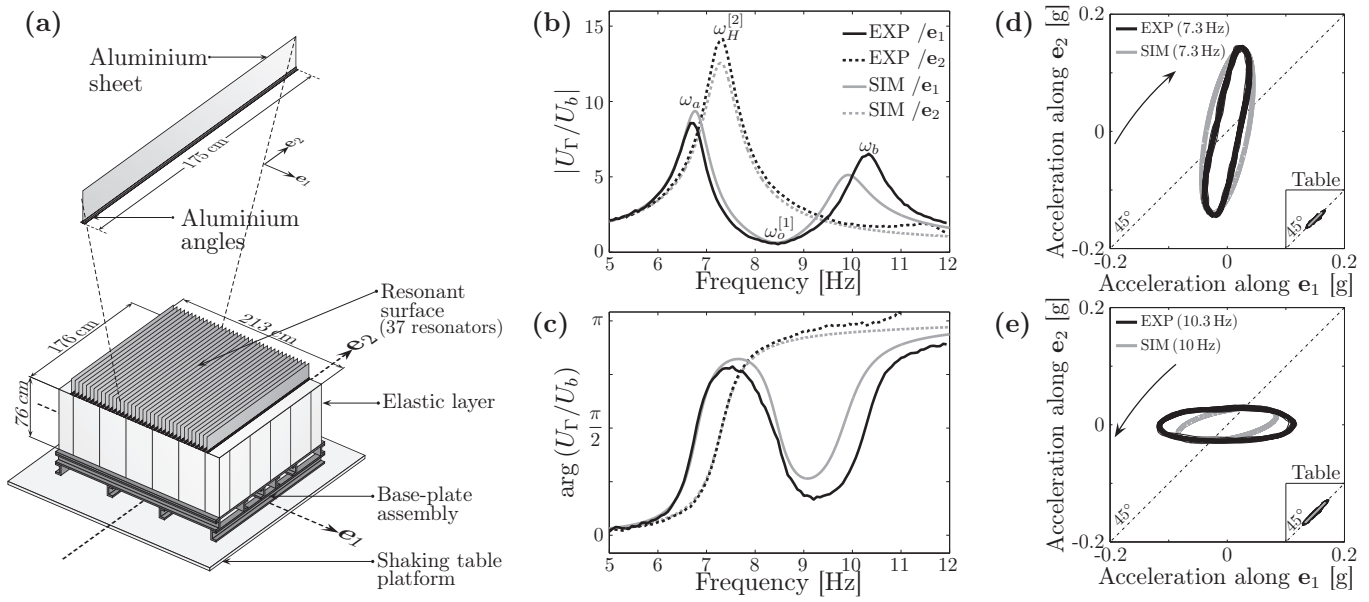

FIGURE 1 – (a) : Experimental prototype. (b) and (c) : Amplitude and phase of the normalized surface motion in the principal axes against frequency. (d) and (e) : Surface motion in response to a harmonic motion prescribed at the table in the 45^o direction from $\mathbf{e}_1$. Comparison between experimental data from central accelerometer (EXP) and theoretical results from Surface Impedance Model (SIM).

sheet remains inert, leading to the inert and modal masses $m_i^{[2]} = m_t$ and $m_o^{[2]} = 0$ and eigenfrequency $\omega_o^{[2]} \lll \omega_o^{[1]}$.

The elastic medium is a layer (thickness $H = 76$ cm) made of cellular polyurethane foam with isotropic linear elastic behaviour (density $\rho = 49$ kg/m^3, shear modulus $\mu = 55$ kPa, Poisson ratio $\nu = 6\%$, shear wave velocity $c_S = 33$ m/s and weak damping $\xi \sim 4.9\%$). The condition of scale separation is satisfied at the resonant surface resonance : $\varepsilon(\omega_o^{[1]}) \approx 0.09$. To magnify interactions, the elastic layer is designed so that its eigenfrequency $\omega_H/(2\pi) = c_S/4H$ in free surface condition is close to the one $\omega_o^{[1]}/(2\pi)$ of the resonant surface. The uniform displacement $\mathbf{U}_b$ is imparted by a shaking table at the base of the layer in the horizontal direction $\mathbf{e}_b$. Denoting $\omega_H^* = \omega_H\sqrt{1-i2\xi}$ and $Z_S^* = \rho c_S\sqrt{1-i2\xi}$, and accounting for the layer thickness H, the surface displacement in the resonant surface principal directions $\mathbf{e}_{j=1,2}$ reads :

$$\frac{\mathbf{U}_\Gamma\cdot\mathbf{e}_j}{\mathbf{U}_b\cdot\mathbf{e}_j} = \left[\cos\left(\frac{\pi}{2}\frac{\omega}{\omega_H^*}\right) + \mathrm{i}\frac{Z_j}{Z_S^*}\sin\left(\frac{\pi}{2}\frac{\omega}{\omega_H^*}\right)\right]^{-1} \qquad (7)$$

where the expression of the resonant surface impedance $\mathbf{Z}_\Gamma = \sum_j Z_j\mathbf{e}_j\otimes\mathbf{e}_j$ is found from Newton's Second Law :

$$\frac{Z_j}{Z_S^*} = \frac{\mathrm{i}\omega m_o^{[j]}}{Z_S^*|\Sigma|}\frac{\omega_o^{[j]2} - \mathrm{i}2\xi_o\omega_o^{[j]}\omega}{\omega_o^{[j]2} - \mathrm{i}2\xi_o\omega_o^{[j]}\omega - \omega^2} + \frac{\mathrm{i}\omega m_i^{[j]}}{Z_S^*|\Sigma|}, \qquad (8)$$

3.2 Evidence of depolarization

The surface displacement in the principal axes is plotted against frequency in Fig. 1(b) and (c) when the base motion $\mathbf{U}_b$ is oriented along $\mathbf{e}_1$ or $\mathbf{e}_2$. Close to the frequency ω_H at which the layer's resonance should be, the resonant surface resonance enforces a rigid-like condition leading to $\mathbf{U}_\Gamma.\mathbf{e}_1 \to 0$ at $\omega = \omega_o \approx \omega_H$. The layer's resonant peak is split into two layer/resonant surface resonant peaks with substantially-reduced amplitudes : at the lower frequency ω_a, the oscillators are in phase with the layer and at the higher frequency ω_b the oscillators are in phase-opposition with the layer. Conversely, when the base motion is oriented along $\mathbf{e}_2$, the transfer function is similar to that of the layer with a free surface but with a reduced eigenfrequency $\omega_H^{[2]}$ due to the inert mass m_t. These experimental observations are in agreement with the theory. This demonstrates the ability of resonant surface to produce boundary conditions ranging from free to rigid-like according to the frequency.

Harmonic horizontal motions $\mathbf{U}_b = U_b\mathbf{e}_{\pi/4}$ are now imposed out of principal axis, with a polarization angle $\pi/4$ counted from $\mathbf{e}_1$. Fig. 1(d) and (e) show that the surface motion $\mathbf{U}_\Gamma$ can strongly depart from the direction of the input motion $\mathbf{U}_b$. In the frequency range $\omega \approx \omega_o^{[1]}$, the response spectrum along $\mathbf{e}_1$ is close to zero due to the resonant surface resonance, while that along $\mathbf{e}_2$ is amplified by the layer resonance around $\omega_H^{[2]}$; hence, the surface motion is mostly polarized along $\mathbf{e}_2$, see Fig. 1(d). In the frequency range $\omega \approx \omega_b$, the response spectrum along $\mathbf{e}_1$ is amplified by the second layer/resonant surface resonance, while that along $\mathbf{e}_2$ has passed the resonance ; hence, the surface motion is mostly polarized along $\mathbf{e}_1$, see Fig. 1(e). These observations agree with the theory and confirm that the resonant surface is a mechanical depolarizer of shear waves.

4 Acoustic resonant surface

To observe the unconventional reflection properties of acoustic resonant surfaces, an experimental prototype is designed using the homogenization model, and both impedance tube and anechoic chamber measurements are compared to the theoretical results. The model is also validated against numerical simulations in a 2D problem with split ring resonators in order to show that critical coupling between the resonant surface and the wavefield can be achieved at the resonance frequency of the resonant surface.

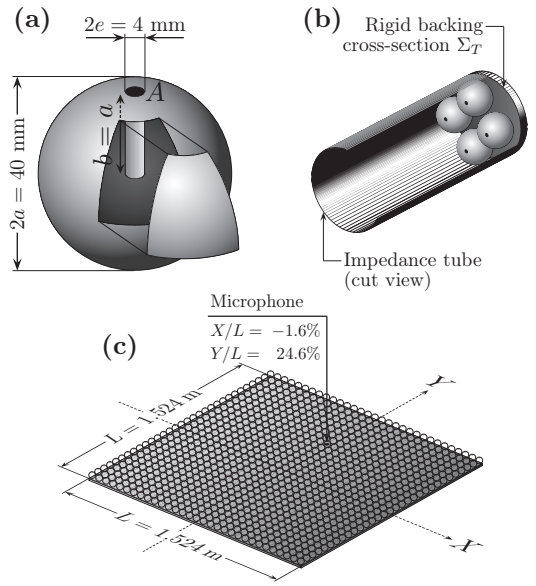

FIGURE 2 – Experimental prototypes. (a) Schematic view of the spherical Helmholtz resonator with details of its inner duct ; (b) Arrangement of 4 Helmholtz resonators in the impedance tube ; (c) Arrangement of 961 Helmholtz resonators on a rigid surface tested in the anechoic chamber.

4.1 Experimental prototype

The resonant surface consists of Helmholtz resonators arranged periodically on a rigid surface. The design developed in [7] to achieve the scale separation around resonance is used. The resonator consists of a spherical cavity of radius $a = 2\ cm$, having a circular opening A with diameter $e = 4mm$ and a long straight inner duct with diameter $e = 4mm$ and length $b = 2cm$, see Fig. 2(a). It behaves as a SDOF oscillator with the mass $m_o = \rho_e|A|b$ and stiffness $k_o = \gamma P_e|A|^2/V$, where $V = 4\pi a^3/3 - |A|b$ is the net volume of the cavity. That provides the theoretical estimate $(2\pi)^{-1}\sqrt{k_o/m_o} \approx 238Hz$ for the eigenfrequency.

4.2 Impedance tube measurements

Measurements in an impedance tube (*B&K* type 4206, circular cross-section Σ_T, diameter $D = 10$cm) are performed on $N = 4$ resonators secured at the rigid end of the tube with their apertures facing up, see Fig. 2(b). A boundary layer analysis leads to the effective boundary condition $\mathbf{v}\cdot\mathbf{n} = \Upsilon p$ for waves in the tube, where Σ_T plays the role of the period Σ, and $\Upsilon = -NY/|\Sigma_T|$. The resonator admittance Y reads :

$$Y = \frac{|A|^2}{m_o\omega_o}\frac{\mathrm{i}\omega_o\omega}{\omega_o^2 - \mathrm{i}2\xi_o\omega_o\omega - \omega^2} \qquad (9)$$

Experiments with a single resonator provide $\omega_o/2\pi \approx 253Hz$ and $\xi_o \approx 6.6\%$ that are used in the model. Results are shown in Fig. 3(a,b). It is confirmed that the resonance leads to a decrease in amplitude of the reflection coefficient (at resonance, the absorption coefficient is $\alpha = 1 - |R|^2 \approx 0.9$) and a phase shift. Analogous measurements with 4 rigid spheres reveal a nearly-total reflection, as expected (no flux produced). The model is accurate despite the poor scale separation $\epsilon_T = \omega_o D/c \approx 0.46$, where $c = 342$ m/s is the sound speed. Note that the roughness induced by the resonators leads to a small phase-shift ($< \pi/12 = O(\epsilon_T)$) neglected in the model at the leading order.

4.3 Anechoic chamber measurements

Anechoic chamber measurements are performed on an array of $31 \times 31 = 961$ Helmholtz resonators (identical to those used in the impedance tube) arranged periodically in a square lattice (spacing $\ell = 5cm$) on a square rigid board (width $L = 1.524m$, thickness $12.7mm$) with their apertures facing up, see Fig 2(c). The scale separation is satisfied at resonance ($\epsilon_o = \ell\omega_o/c \approx 0.23$). The source is positioned above the centre of the board, at the distance $H = 2.47m$. The insertion loss $IL = -10\log|p_\Gamma/p_0|^2$ is shown in Figure 3(c), where p_Γ and p_0 are the pressure recorded at the surface with and without the resonators. As expected, the resonance leads to a sound attenuation at the surface ($IL \approx 3.7$ dB at resonance) related to the absorption of the incident field (absorption coefficient $\alpha \approx 0.9$). Due to the quasi-normal incidence of the wavefront on the board, the data is compared with theoretical results for plane wave reflection in normal incidence. The model predictions ($IL = -10\log|(1+R)/2|^2$, with $R = [1-\rho_e c\Upsilon]/[1+\rho_e c\Upsilon]$), are in good agreement with the data.

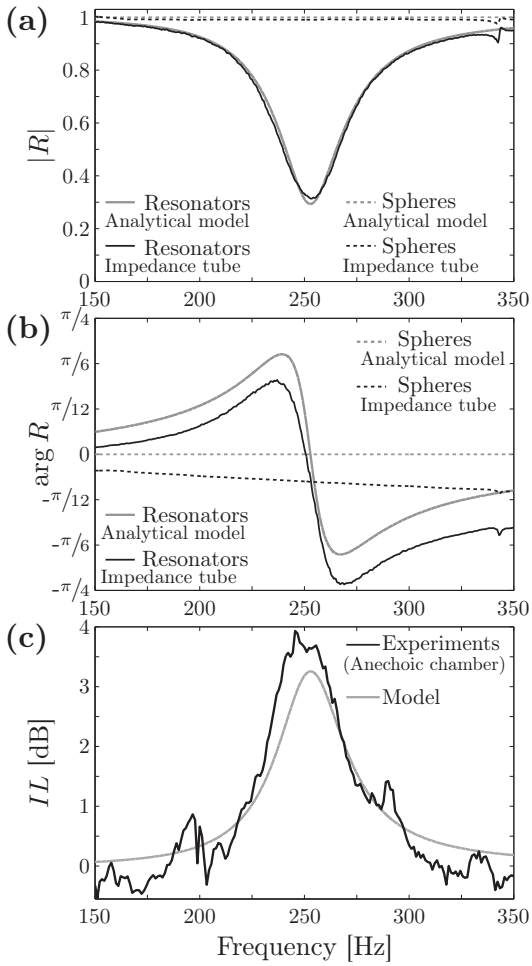

FIGURE 3 – Experimental results compared with the model predictions. (a) amplitude and (b) phase of the reflection coefficient from impedance tube measurements on 4 resonators or 4 rigid spheres. (c) Insertion loss from anechoic chamber measurements on 31×31 resonators.

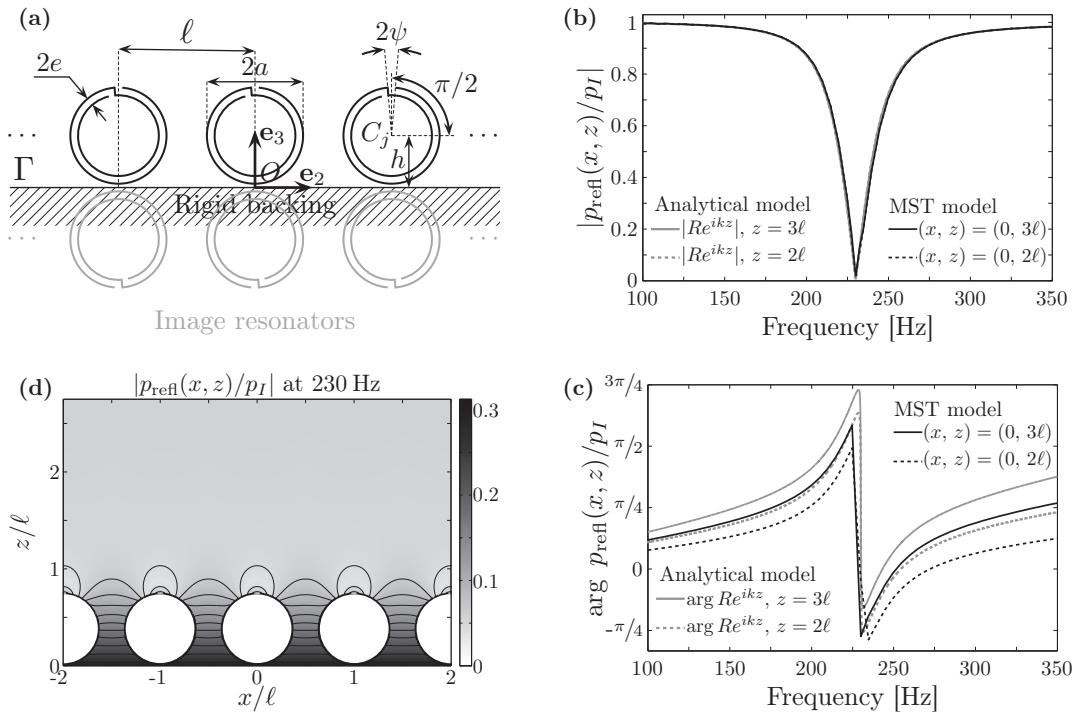

FIGURE 4 – Numerical model in 2-D and comparison with analytical results. (a) geometry of the resonant surface ; (b) amplitude and (c) phase of the reflected field against frequency at the distance $z = \mathbf{x} \cdot \mathbf{n}$ above the surface ; (d) spatial distribution of the reflected field at the frequency of resonance. Fields are normalized to the incident amplitude p_I.

4.4 Numerical validation in 2-D

If the critical coupling $\rho_e c\Upsilon = 1$ is achieved at some frequency, the homogenization model predicts a total absorption of a normally-incident plane wave. In order to investigate this effect, a case study is performed using resonators in the form of slotted cylinders. When sufficiently long, they can be modelled as 2-D Helmholtz resonators and the Multiple Scattering Theory (MST) can be applied to solve the problem numerically. The case study deals with the reflection of the normally-incident plane wave $P_I = p_I \exp(-i\omega \mathbf{e}_3 \cdot \mathbf{x}/c)$ from a rigid surface Γ upon which the 2D Helmholtz resonators are arranged ℓ-periodically, see Fig. 4(a). Resonators (labelled by $j \in \mathbb{Z}$ integer) have a circular cross section with radius $a = 2.5cm$, a slot facing up with the width $2e = 4mm$ (angular opening $2\psi = 2e/a$) and the spacing $\ell = 7cm$. The resonators' centre C_j are at the distance $h = 2.7cm$ from the surface Γ (note $h + a < \ell$). The boundary of the resonator is rigid, except for the slot where the following conditions are applied : the radial component of the particle velocity is uniform and equal to $v_{\text{slot}} = (Y/|A|)\langle p_{\text{tot}}\rangle$ where $\langle p_{\text{tot}}\rangle$ is the mean pressure over the slot. Inside, the Helmholtz resonator has a perimeter-long, 4mm-wide duct wrapped around the cavity, see Figure 4(a). A Finite Element Model provides $\omega_o/2\pi \approx 230$ Hz (basic mass-spring analysis provide 250Hz). The design is such that the scale separation is satisfied ($\epsilon_o = \ell\omega_o/c \approx 0.29$) and a damping $\xi_o = 4\%$ is assumed so that $\rho_e c\Upsilon = 1$ at the resonance frequency.

Following MST procedure (for instance [8, 9]), the total pressure field is decomposed into $p_{\text{tot}} = P_I + P_R + p_{\text{scat}}$ where $P_R = p_I \exp(i\omega \mathbf{n} \cdot \mathbf{x}/c)$ is the field reflected from the rigid surface Γ were the resonators removed and $p_{\text{scat}} = \sum_j (p_j + \widetilde{p_j})$ is the field scattered by the resonators array : p_j is scattered by the (physical) resonator j and $\widetilde{p_j}$ by its mirror-image from the rigid surface Γ. Due to the periodicity, the contributions of all resonators j to the scattered field are equal so that, in the local polar coordinate system (C_j, r_j, θ_j) centred on j (angle θ_j is counted from $\mathbf{e}_2$) :

$$p_j(r_j, \theta_j) = \sum_{n\in\mathbb{Z}} A_n H_n(kr_j) e^{in\theta_j} \tag{10}$$

where H_n is the Hankel function of the first kind and order n and A_n are complex amplitudes (independent from j). Because of the mirror-image symmetry, $\widetilde{p_j}(\widetilde{r_j}, \widetilde{\theta_j}) = p_j(\widetilde{r_j}, -\widetilde{\theta_j})$ in the polar coordinate system $(\widetilde{C_j}, \widetilde{r_j}, \widetilde{\theta_j})$ associated with the image-resonator j. The coefficients A_n are found from the boundary conditions applied to the resonator $j = 0$. To do so, the fields are expanded in the coordinate system $(C, r, \theta) = (C_0, r_0, \theta_0)$ using the Jacobi-Anger expansion [10] :

$$\{P_I + P_R\}(r, \theta) = \sum_{n\in\mathbb{Z}} U_n J_n(kr) e^{in\theta} \tag{11}$$

where $U_n = \left\{e^{+ikh} + (-1)^n e^{-ikh}\right\}$ and J_n is the Bessel function of the first kind and order n. Using Graf's addition theorem [10] for resonators $j \neq 0$:

$$p_j(r, \theta) = \sum_{n\in\mathbb{Z}} \sum_{m\in\mathbb{Z}} C_j^{nm} A_m J_n(kr) e^{in\theta} \tag{12}$$

and similarly for $\widetilde{p_j}(r, \theta)$ with coefficients $\widetilde{C_j^{nm}}$, where :

$$C_j^{nm} = H_{m-n}(k\sqrt{(j\ell)^2}) e^{i(m-n)(\beta_j + \pi)} \tag{13a}$$

$$\widetilde{C_j^{nm}} = H_{m+n}(k\sqrt{(j\ell)^2 + 4h^2}) e^{-i(m+n)\widetilde{\beta_j} + im\pi} \tag{13b}$$

and β_j (resp. $\widetilde{\beta_j}$) is the angle between $\mathbf{e}_2$ and CC_j (resp. $C\widetilde{C_j}$). The radial component of the velocity $\mathbf{v}_{\text{tot}} = \mathbf{grad}(p_{\text{tot}})/i\omega\rho_e$

at the boundary $r = a$ is expanded using Fourier decomposition, providing :

$$\frac{\partial}{\partial r}\frac{p_{\text{tot}}}{i\omega\rho_e}\bigg|_a = \sum_{n\in\mathbb{Z}} \frac{Y}{|A|}\langle p_{\text{tot}}\rangle \frac{\sin(n\psi)}{n\pi} e^{in(\theta-\frac{\pi}{2})} \qquad (14)$$

Due to orthogonality, boundary conditions can be formulated separately for each harmonic $e^{in\theta}$. This leads to an infinite system of equations for the unknown coefficients A_n, which is solved numerically by truncation. This gives the pressure $p_{\text{refl}} = P_R + p_{\text{scat}}$ of the wave reflected from the array.

The field p_{refl} is computed above the resonator $j = 0$ (abscissa $x = \mathbf{x}\cdot\mathbf{e}_2 = 0$) and at the distance $z = \{2\ell, 3\ell\}$ above the surface Γ. It is compared in Fig. 4(b,c) with the analytical model predictions $p_R = Re^{ikz}$. A good agreement between the MST and the analytical model confirms the phenomenon of a nearly total absorption at resonance. A small discrepancy in the phase of the reflected field is due to the surface roughness ; a similar discrepancy of the analytical model with measurements has been noted in Section 4.2. Finally, the spatial distribution of the pressure p_{refl} is presented in Figure 4(d) at the frequency of resonance and confirms the existence of the periodic boundary layer. In accordance with the analytical model, its amplitude is $O(\epsilon p_I)$ and it is confined in the close vicinity of the surface array, with a characteristic distance of evanescence $O(\ell)$.

5 Conclusion

The characteristic feature of resonant surfaces is the coincidence within the same frequency range of : long wavelength dynamics in the supporting layer ; and local dynamics of the periodically distributed resonators. The fact that micro-structured materials can show anomalous properties when inner resonances are involved has been demonstrated as early as 1985 in elastodynamics [11], and has since found numerous applications in many branches of physics with the development of so-called metamaterials. In this sense, resonant surfaces may be seen as a 2D-version of metamaterials, that is metasurfaces. Experimental evidence has been obtained of the efficiency of resonant surfaces to control wavefields in homogeneous media, and in particular that of elastodynamic resonant surface to depolarize mechanical waves. In elastodynamics, results can be applied to systems from nanoscale [12], using nanotubes to stabilize their substrate, to geophysical scale [13, 14], taking into account the presence of high-rise buildings in seismic engineering. Obvious applications in acoustics and elastodynamics include noise absorption and wavefield manipulations.

Remerciements

The authors are also grateful to C. Taylor, P-Y. Bard, L. Padrón, E. Skuse, D. Ward, F. Sallet, A. Tomlinson, H.-C. Shin, S. Taherzadeh and K. Attenborough for their active contribution in the projects. The research leading to the results in elastodynamics has received funding from the European Community's Seventh Framework Program [FP7/2007-2013] for access to the University of Bristol's Earthquake and Large Structures (EQUALS) Laboratory under grant agreement n°227887. The research leading to the results in acoustics has been supported by the U.K. Engineering and Physical Sciences Research Council (grant agreements EP/K037234/1 and EP/K03720X/1).

Références

[1] E. Sanchez-Palencia, *Non-Homogeneous Media and Vibration Theory*. Lectures Notes in Physics, Vol. 127, Springer-Verlag, Berlin Heidelberg (1980).

[2] J.-L. Auriault, C. Boutin and C. Geindreau, *Homogenization of Coupled Phenomena in Heterogenous Media*, ISTE Ltd and John Wiley & Sons, Inc. (2009).

[3] C. Boutin and P. Roussillon, Wave propagation in presence of oscillators on the free surface. *Int. J. of Eng. Science* **44**, 180-204 (2006).

[4] L. Schwan, O. Umnova, C. Boutin, H.-C. Shin, S. Taherzadeh and K. Attenborough, Acoustic resonant surface : from nearly-total reflection to nearly-total absorption of sound, *Proceedings of the EuroNoise*, 977–982 (2015).

[5] L. Schwan and C. Boutin, Unconventional wave reflection due to 'resonant surface', *Wave Motion* **50**, 852-868 (2013).

[6] C. Boutin and L. Schwan, Elastodynamic metasurface : Depolarization of mechanical waves and time effects, *Journal of Applied Physics* **117**, 064902 (2015).

[7] C. Boutin, Acoustics of porous media with inner resonators. *J. Acoust. Soc. Am.* **134**, 4717-4729 (2013).

[8] A. Krynkin, O. Umnova, A. Y. B. Chong, S. Taherzadeh and K. Attenborough, Scattering by coupled resonating elements in air. *J. Phys. D : Appl. Phys.* **44**, 125501 (2011).

[9] A. Krynkin, O. Umnova, J. V. Sánchez-Pérez, A. Y. B. Chong, S. Taherzadeh, and K. Attenborough, Acoustic insertion loss due to two dimensional periodic arrays of circular cylinders parallel to a nearby surface. *J. Acoust. Soc. Am.***130**, 3736-3745 (2011).

[10] H. Bateman and A. Erdelyi, *Higher Transcendental Functions*, McGraw-Hill Book Company (1953).

[11] J. L. Auriault and G. Bonnet, Dynamique des composites élastiques périodiques, *Arch. Mech.* **37**, 269-284 (1985).

[12] V. Eremeyev, E. Ivanova, N. Morozov and S. Strochkov, Method of determining the eigenfrequencies of an ordered system of nanoobjects, *Technical Physics* **52**, 1-6 (2007).

[13] A. Wirgin and P.-Y. Bard, Effects of building on the duration and amplitude of ground motion in Mexico City, *Bull. Seis. Soc. Am.* **86**, 914-920 (1994).

[14] L. Schwan, C. Boutin, L. Padrón, M. S. Dietz, P.-Y. Bard and C. Taylor, Site-city interaction : Theoretical, numerical and experimental crossed-analysis, *Geophys. J. Int.*, In press, (2016).